

1 **Deep-water osmium-isotope record of the Permian–Triassic interval from**
2 **Niushan, China reveals potential delayed volcanic signal post the mass extinction**

3 **Zeyang Liu^{1,2,3}, David Selby^{3,4}**

4 ¹State Key Laboratory of Organic Geochemistry, Guangzhou Institute of Geochemistry,
5 Chinese Academy of Sciences, Guangzhou 510640, China

6 ²CAS Center for Excellence in Deep Earth Science, Guangzhou, 510640, China

7 ³Department of Earth Sciences, Durham University, Durham DH1 3LE, UK

8 ⁴State Key Laboratory of Geological Processes and Mineral Resources, School of Earth
9 Resources, China University of Geosciences, Wuhan, 430074, Hubei, China

10 Corresponding author: Zeyang Liu (geozy.liu@outlook.com)

11 **Abstract**

12 The end Permian mass extinction event is one of the most severe biotic crisis of the Phanerozoic.
13 The trigger of this event has been widely linked to massive volcanic activity associated with
14 the Siberian Traps Large Igneous Province through the application of multiple
15 geochronological (e.g., U-Pb and Ar-Ar dating) and geochemical proxies (e.g., C, Hg, Zn, Os,
16 etc.). Of these proxies, a few osmium ($^{187}\text{Os}/^{188}\text{Os}$) records are available for near-shore /
17 shallow water depositional settings (e.g., Meishan, China; Opal Creek, Canada), which suggest
18 multiple episodes of volcanism before, during and after the mass extinction event. Here, we
19 present a new initial $^{187}\text{Os}/^{188}\text{Os}$ (Os_i) stratigraphy across the deep-water Niushan Permian–
20 Triassic boundary interval section of South China that reveals a single unradiogenic Os-isotope
21 shift (from ~ 0.6 to 0.3) after the end Permian mass extinction event interval, which is
22 interpreted to be related to volcanic activity. Above the unradiogenic excursion, a radiogenic
23 shift to ~ 1.1 is detected across the Permian–Triassic boundary at Niushan that is correlative to
24 the radiogenic Os_i shift observed in the Meishan section. This increase in Os-isotope values is
25 taken to reflect enhanced continental weathering. Both the unradiogenic and radiogenic
26 excursions in the deep-water Niushan section are smaller in magnitude compared with the Os
27 isotope profiles from more shallow-water sections of Meishan and Opal Creek. Our data
28 suggest investigations of multiple sections across a variety of depositional environments may
29 yield a more comprehensive understanding of the scale of the global perturbations related to
30 volcanism and continental weathering intensity of the Permian–Triassic boundary interval.

31 **Keywords:** Osmium isotope, end Permian mass extinction, volcanism, weathering, South
32 China

33 **1 Introduction**

34 The end Permian mass extinction (EPME) event represents the most severe biotic loss
35 of both marine and terrestrial species of the Phanerozoic (Erwin, 2006). This biotic crisis is
36 associated with an intense disturbance in the global carbon cycle that is characterized
37 worldwide by sedimentary sections exhibiting large negative carbon isotope excursions (see a
38 review by Korte and Kozur, 2010). Further, during the EPME the Earth's environment
39 witnessed global warming (Joachimski et al., 2012; Sun et al., 2012; Chen et al., 2016), oceanic
40 acidification (Hinojosa et al., 2012; Clarkson et al., 2015; Garbelli et al., 2017; Song et al.,
41 2021), and oceanic anoxia and/or euxinia (Wignall and Twitchett, 1996; Grice et al., 2005; Cao
42 et al., 2009). These environmental perturbations and the mass extinction have been ultimately
43 linked to intensive volcanism associated with the Siberian Traps Large Igneous Province (LIP)
44 (e.g. Payne and Kump, 2007; Saunders and Reichow, 2009; Shen et al., 2013; Hu et al., 2019;
45 Shen et al., 2019b).

46 Being the largest mass extinction event, the end Permian mass extinction event and the
47 Permian–Triassic boundary (PTB) interval have been extensively studied by high-resolution
48 biostratigraphy, high-precision dating and isotope stratigraphy (e.g. mercury and zinc isotopes;
49 Liu et al., 2017; Wang et al., 2018, Shen et al., 2019a; Chu et al., 2020; Dal Corso et al., 2020).
50 To date, osmium-isotope ($^{187}\text{Os}/^{188}\text{Os}$) stratigraphy for the Permian–Triassic interval are
51 limited to the Meishan (South China) and Opal Creek (Canada) sections (Schoepfer et al., 2013;
52 Georgiev et al., 2015; Zhao et al., 2015; Liu et al., 2020b). Osmium isotope data of the
53 Permian–Triassic interval are also reported for the Hovea-3 section (Western Australia),
54 however, absolute interpretation of the data suffers from potential disconformity and
55 uncertainty in the position of the Permian–Triassic boundary (Georgiev et al., 2020).

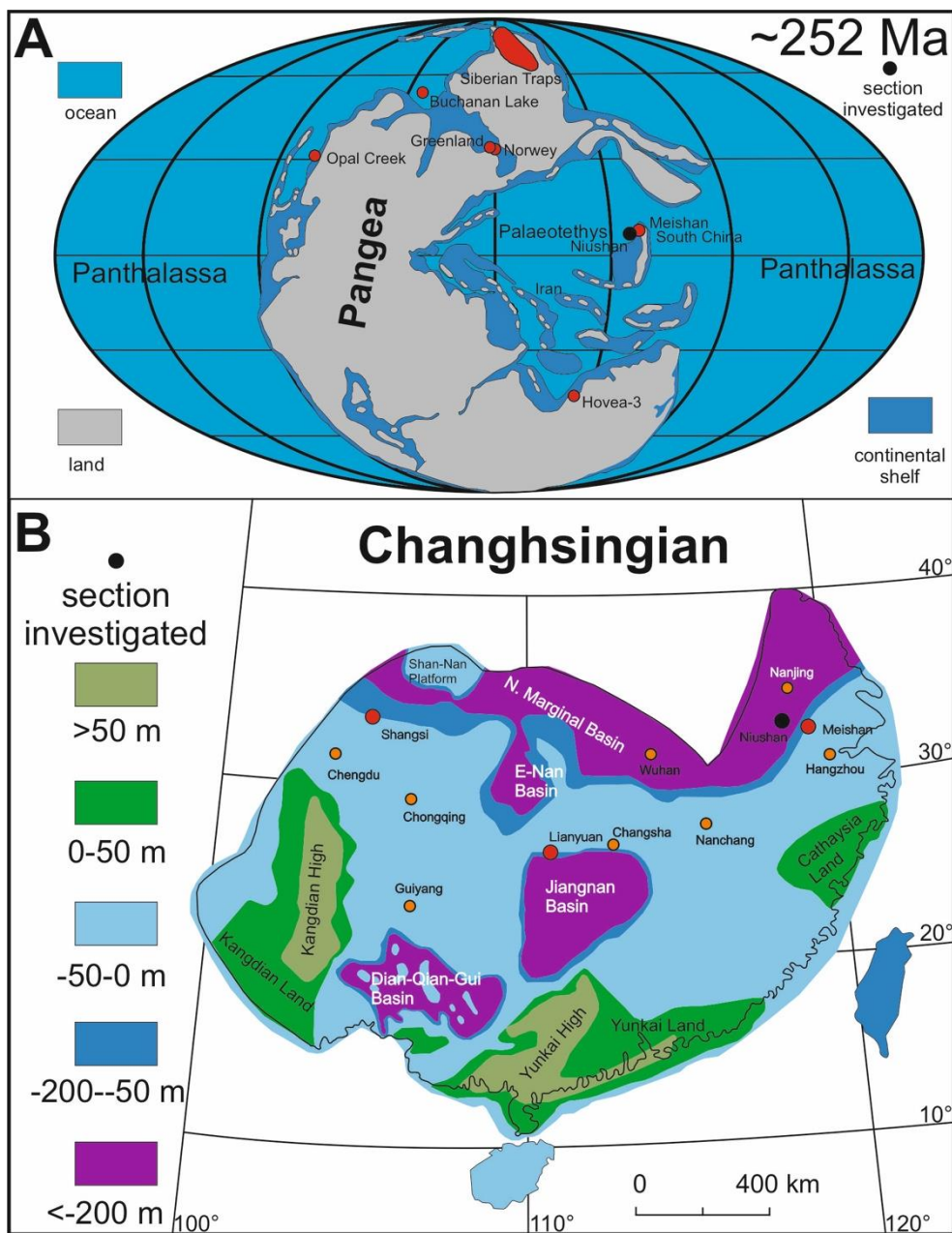
56 The Meishan section hosts the Global Stratotype Section and Points (GSSPs) for the
57 Permian–Triassic boundary and the Wuchiapingian–Changhsingian boundary (Yin et al., 2001;
58 Jin et al., 2006). This section was deposited in a middle–upper slope setting, with an estimated
59 water depth between 30–60 m (Yin et al., 2001). The Opal Creek section represents an outer-
60 shelf or upper slope setting on the eastern of the Panthalassa Ocean at a paleolatitude of ~ 30°N
61 (Henderson, 1989). A major regional unconformity is placed ~ 1.5 m below the Permian–
62 Triassic boundary that separates the lower Middle Permian strata from the upper Upper
63 Permian–Lower Triassic deposits.

64 Previous paleoclimate studies using Os isotopes suggest that, in response to geological
65 events, Os isotope stratigraphy from different paleogeographic depositional settings may
66 express discrete Os isotope composition and different magnitudes of isotope excursion (e.g.
67 Paquay and Ravizza, 2012; Rooney et al., 2016; Liu et al., 2019b; Jones et al., 2020). In this
68 study, we report osmium isotope stratigraphy for the Permian–Triassic boundary interval from
69 the deep-water section Niushan section (South China), to provide further insights into the
70 temporal relationship and magnitude of the volcanism and subsequent climate perturbation.

71 **2 Geological background**

72 The Niushan section outcrops in an active quarry located in Xuancheng City, Anhui
73 Province (N31°08'57.6", E118°49'44.9"; Fig. 1 and 2). The section comprises the Longtan,
74 Dalong, and Yinkeng formations, and is constrained biostratigraphically by the occurrence of
75 early Triassic ammonoids (Ophiceratidae) that occur immediately above a volcanic ash layer
76 (Ash-6 in Fig. 2), and geochronologically by LA-ICP-MS U-Pb zircon ages (Fig. 2; Liao et al.,
77 2016a). The correlation of the section with the Meishan section is further supported by a high-
78 resolution organic carbon isotope stratigraphy (Liao et al., 2016a). Sample NS-107 records the
79 lowest $\delta^{13}\text{C}_{\text{org}}$ in the Niushan section, and correlates to the extremely negative carbon isotope

80 excursions in bed 26 of the Meishan section. Moreover, abundant calcareous and siliceous
 81 organisms (e. g., brachiopods) occur below, but not above NS-107, indicating a dramatic biotic
 82 abundance decrease across this interval (Liao et al., 2016a).



83
 84 **Figure 1.** Late Permian paleogeographic maps showing the studied areas. (A) Changhsingian
 85 Stage global paleogeographic reconstruction map showing the location of the Niushan,
 86 Meishan, Greenland, Norway, Buchanan Lake, Hovea-3 and Opal Creek sections; base map
 87 after Ziegler et al. (1997); (B) South China showing the paleogeographic locations of the

88 Niushan (black circle) and Meishan, Shangsi, Lianyuan (red circle) sections; base map
89 modified from Wang and Jin (2000). Figure modified from Liu et al. (2019b).

90 The lower part of the section is recorded by the Longtan Formation which is composed
91 of silty sandstone that is interbedded with thin coal beds in its lower part. Conformably
92 overlying the Longtan Formation is the Dalong Formation that is dominated by organic-rich
93 thin to medium bedded calcareous and siliceous shale, with thin interbeds of carbonate and
94 chert. The Dalong Formation is conformably overlain by the Yinkeng Formation, which
95 comprises mainly dark grey mudstone in its lower part and carbonate rocks in its upper part.
96 Several volcanic ash layers occur in the upper Dalong and lower Yinkeng formations (Fig. 2).
97 Four of these have been dated by U-Pb zircon LA-ICP-MS to be 251.74 ± 0.77 Ma, $251.70 \pm$
98 0.97 Ma, 252.20 ± 1.80 Ma and 252.49 ± 0.76 Ma (Fig. 2; Liao et al., 2016a; 2016b). The
99 Permian–Triassic boundary is assigned to the lower part of the Yinkeng Formation. The end
100 Permian mass extinction interval is characterized by a large negative carbon isotope excursion
101 of ~ 3 ‰ ($\delta^{13}\text{C}_{\text{org}}$) that is correlative to $\delta^{13}\text{C}_{\text{carb}}$ and $\delta^{13}\text{C}_{\text{org}}$ profiles from other EPME sections
102 globally. The Longtan, Dalong and Yinkeng formations of the Niushan section reflect a
103 regional rise in sea level, with the paleoceanographic reconstruction of the WCB interval
104 representing a fluvial/deltaic deposition and the PTB interval interpreted to record a deep-water
105 setting with water depths >200 m (Fig. 1; Wang and Jin, 2000), which is in contrast to the
106 Meishan section that represents a shallow/middle-upper slope depositional setting (<200 m;
107 Wang and Jin, 2000). Present day the distance between the Niushan and Meishan sections is
108 90 Km. Given that no tectonism has occurred since deposition to bring the sites geographically
109 closer, it is considered that the depositional environments/settings of the Meishan (shallow-
110 water section) and Niushan (deep-water section) were of similar distance apart as they are
111 present day.

112 3 Methods

113 Samples (n = 23) from the Niushan section were obtained from archived samples that
114 were collected as part of a previous study from a freshly exposed quarry face at Niushan (Liao
115 et al., 2016a). According to the zircon U-Pb age chronology and the carbon isotope stratigraphy
116 of the section, sampling was aimed to encapsulate the pre, syn and post EPME interval.
117 Samples were not collected adjacent to the stratigraphically distinct ash horizons to avoid any
118 potential contamination of hydrogenous Re and Os with volcanic Re and Os in the sedimentary
119 units. Each sample represents a stratigraphic interval of 1 cm. Approximately 30 g of each
120 sample were polished using silicon carbide grit and milli-Q water to eliminate any
121 contamination potentially introduced from cutting using a diamond-tipped blade. The samples
122 were rinsed with ethanol prior to drying in an oven at 60°C for ~12 hours (overnight). The
123 dried sample was then broken into chips and crushed to a fine powder (~30 µm) with no metal
124 contact using a zirconia ceramic dish and puck.

125 The rhenium-osmium (Re–Os) isotope analysis was carried out at the Durham
126 Geochemistry Centre (Laboratory for Sulfide and Source Rock Geochronology and
127 Geochemistry, and Arthur Holmes Laboratory) at Durham University. The analytical protocol
128 utilises the Cr^{VI}–H₂SO₄ digestion methodology to preferentially liberate hydrogenous Re and
129 Os, and to limit incorporation of any detrital Re and Os (Selby and Creaser, 2003).
130 Approximately 1 g of sample powder with a known amount of mixed ¹⁹⁰Os and ¹⁸⁵Re tracer
131 (spike) solution and 8 ml of 0.25 g/g Cr^{VI}–H₂SO₄ solution were placed and sealed in to a carius
132 tube and heated at 220°C for 48 h. Osmium was purified by solvent extraction (CHCl₃) and
133 micro-distillation methods (Cohen and Waters, 1996; Birck et al., 1997). Rhenium was
134 separated and purified from the Os-extracted Cr^{VI}–H₂SO₄ solution using NaOH–C₃H₆O solvent
135 extraction and anion chromatography. The purified Re and Os fractions were loaded onto Ni
136 and Pt filaments, respectively (Selby et al., 2007). Isotopic measurements were determined

137 using a ThermoScientific TRITON mass spectrometer using static Faraday collection for Re
138 and secondary electron multiplier in peak-hopping mode for Os. Total procedural blanks during
139 this study were 15.6 ± 0.45 pg and 0.035 ± 0.007 pg (1σ S.D., $n = 3$) for Re and Os, respectively,
140 with an average $^{187}\text{Os}/^{188}\text{Os}$ value of 0.18 ± 0.01 . Blank contributes less than 1 % of the Re and
141 Os budget, except for 7 samples, of which 6 are of Early Triassic age that have blank
142 corrections of up to ~ 20 %.

143 The initial $^{187}\text{Os}/^{188}\text{Os}$ composition (Os_i) were calculated using the ^{187}Re decay constant
144 $1.666 \times 10^{-11} \text{yr}^{-1}$ (Smoliar et al., 1996). Due to the relatively large uncertainties of the LA-ICP-
145 MS ages of the volcanic ashes (Liao et al., 2016a; 2016b), each sample's age was estimated
146 using the geochronology of the Wuchiapingian–Changhsingian (254.14 Ma; Shen et al., 2019c)
147 and Permian–Triassic boundaries (251.9 Ma; Shen et al., 2019c), assuming a constant
148 deposition rate throughout the section. The age difference between a sample's real age and the
149 assigned age has negligible effect on the calculated Os isotope initial (Os_i). For example, a 0.5
150 Myr age difference results in < 0.02 variation in the calculated Os_i with the exception for a few
151 samples in the lower part of the section that have higher Re/Os ratios. For these samples the
152 difference in the calculated Os_i can be up to 0.05. Repeat analyses of reference material SDO-
153 1 suggest ≤ 0.04 variation in calculated Os_i (Du Vivier et al., 2014; 2015).

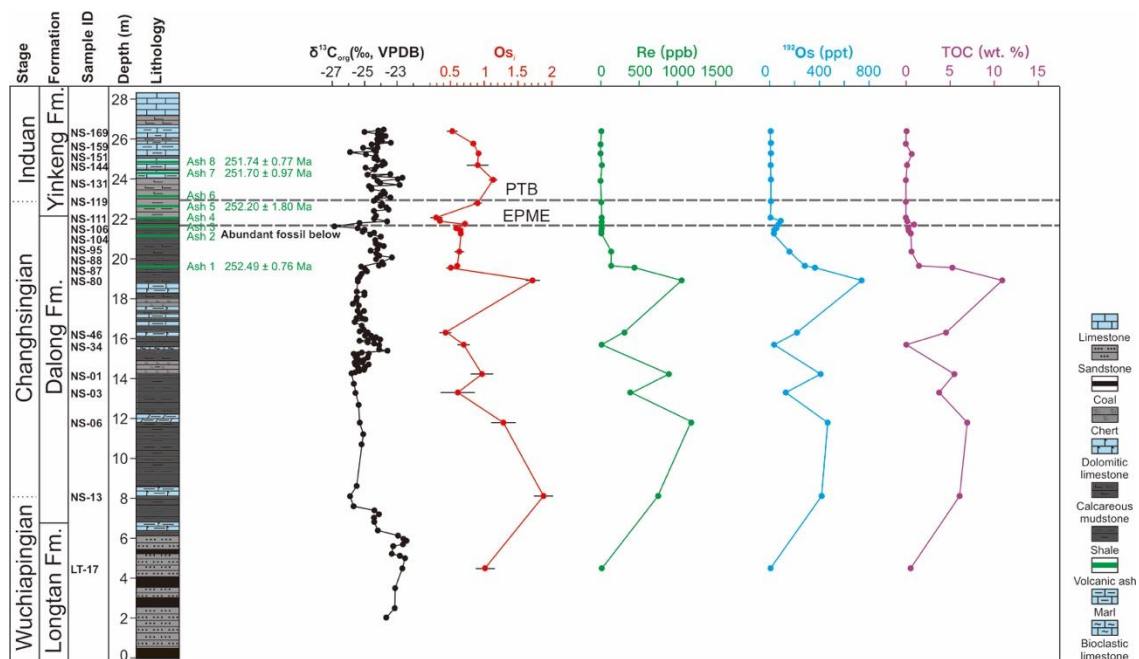
154 **4 Results**

155 The Re and Os concentrations for the Niushan section range from ~ 0.1 to 1192 ppb
156 and 6.2 to 4975 ppt ($^{192}\text{Os} = \sim 2.3 - 738$ ppt), respectively (Table S1; Fig. 2). Stratigraphically,
157 except for the lowest sample in the Longtan Formation, samples within the Dalong Formation
158 ($\sim 7 - 22$ m) are enriched in Re and Os (5.1 – 1191.6 ppb and 155 – 4975 ppt, respectively),
159 with samples in the Yinkeng Formation (above ~ 20 m) exhibiting a decline in Re and Os

160 abundance to less than 1 ppb and 21 ppt, respectively. The trend in Re and Os abundance, in
 161 general follows the trend with total organic carbon (TOC) (Table S1; Fig. 2).

162 In the late Wuchiapingian (upper Longtan and basal Dalong Formations), the two
 163 analysed samples (LT-17, NS-13) yield radiogenic Os_i values (~ 1.0 and 1.9 , respectively) (Fig.
 164 2). The Os_i value is less radiogenic across the middle Changhsingian (middle Dalong Formation,
 165 14-16m) (average of samples NS-01, 03, 34, 46, 0.68 ± 0.23 , $n = 4$). Between the latter and
 166 samples at and above 20 m there is a single sample (NS-80) with a Os_i of 1.72 . Approximately
 167 2 m below to the EPME the Os_i are ~ 0.52 to 0.71 (average 0.62 ± 0.06). Immediately above
 168 the negative carbon-isotope anomaly at the EPME interval two samples with distinctly different
 169 Re (16.9 and 0.7 ppb) and Os (265.5 and 21.0 ppt) have very similar Os_i values (0.30 and 0.34).
 170 The Os_i then rises to 1.14 across the Permian–Triassic boundary, and then returns to 0.53 in
 171 the early Triassic.

172



173

174 **Figure 2.** Carbon isotope ($\delta^{13}C_{org}$, black), Os_i (red), Re (green) and ^{192}Os abundance (blue)
 175 stratigraphy of the Niushan section, China. The $\delta^{13}C_{org}$ data, TOC data, lithology and sea level
 176 curve are from Liao et al. (2016a). Ash layer chronology are LA-ICP-MS U–Pb Zircon ages

177 from Liao et al. (2016a, 2016b). Ages in the column are that used to calculate each sample's
178 Os_i , estimated with the Permian–Triassic boundary age and Wuchiapingian–Changhsingian
179 boundary age, assuming a constant deposition rate throughout the section. EPME = end
180 Permian Mass Extinction; PTB = Permian–Triassic Boundary.

181 **5 Discussion**

182 5.1 Data evaluation

183 The Re-Os system has been shown to be disturbed by post-depositional processes (such
184 as weathering and hydrothermal activity), and some of the samples close to the P–T interval
185 have Re and Os values close to the upper continental crust (0.198 ppb Re and 31 ppt Os;
186 Peucker-Ehrenbrink and Jahn, 2001). However, we suggest that the Os isotope values in the
187 Niushan section represent seawater Os isotope values during the Late Permian and Early
188 Triassic based on the following points: 1) the samples were recovered from an active quarry
189 and therefore collected samples were from a freshly exposed surface; 2) utilized samples
190 showed no visible evidence of veining or weathering; 3) analytical protocol employs a CrO_3 -
191 H_2SO_4 digestion medium that has been shown to preferentially liberate the hydrogenous Re
192 and Os (Selby and Creaser, 2003; Kendall et al., 2004; Rooney et al., 2011; Xu et al., 2012;
193 Sperling et al., 2014), and 4) the Re-Os systematics of stratigraphically adjacent samples (NS-
194 109, NS-111) possessing significantly different Re and Os budgets yield very similar Os_i values.
195 In addition, the calculated Os_i are geologically plausible and similar to previously reported Os_i
196 values from the Late Permian and Early Triassic sections (Yang et al., 2004; Georgiev et al.,
197 2011, 2015; Schoepfer et al., 2013; Zhao et al., 2015; Liu et al., 2020b).

198 5.2 Paleogeographic control of Os_i values

199 The Niushan section records a near-shore delta plain depositional setting during the
200 Wuchiapingian and transition to a marine setting across the Wuchiapingian–Changhsingian

201 boundary interval (Liao et al., 2016a). Both samples in the late Wuchiapingian yield highly
202 radiogenic Os_i values (~ 1 and 1.9). These values are comparable to those reported from the
203 Lianyuan section in South China (~ 1.2), which also records a fluvial-deltaic paleogeographic
204 setting expressed by similar siltstone interbedded with thin coalbeds during this time interval
205 (Liu et al., 2019b). These radiogenic Os_i mainly reflect the proximal continental setting of the
206 sites, with the bulk of its Os being derived from continental runoff, with limited contribution
207 of Os from open-marine seawater. The Os_i increase from 1 to 1.9 may reflect increased
208 restriction in response to a fall in sea level and/or tectonic uplift. In contrast to the radiogenic
209 Os isotope signature of the near-shore Lianyuan and Niushan (South China) sections,
210 Wuchiapingian–Changhsingian sections that were deposited in more marine setting (i.e. the
211 Meishan and Shangsi sections in South China, the Buchanan Lake in Canada, Greenland and
212 Norway sections) generally have a less radiogenic Os isotope composition ($\sim 0.55 - 0.60$;
213 Georgiev et al., 2011; Liu et al., 2019b). Within the marine incursion in the Niushan section,
214 the Os_i values drop to ~ 0.6 in the upper Changhsingian, and these values are equivalent to that
215 of late Permian seawater Os isotope values which are reconstructed from the continental shelf
216 marine sections of Opal Creek (Canada), Hovea-3 (Australia), and Meishan (China) (Schoepfer
217 et al., 2013; Georgiev et al., 2015, 2020; Zhao et al., 2015; Liu et al., 2020b). Another Os_i
218 increase to ~ 1.7 is detected in the upper Changhsingian, which likely reflect another pulse of
219 sea level shallowing, as evidenced by the lithology change from shale to carbonates.

220 5.3 Osmium isotope evidence for volcanism and weathering

221 Available Os isotope data from the Meishan (South China) and Opal Creek (Canada)
222 sections exhibit multiple unradiogenic Os isotope excursions that are interpreted to reflect
223 episodes of volcanic activities before, during and after the EPME (Schoepfer et al., 2013;
224 Georgiev et al., 2015; Liu et al., 2020b). In contrast, the more deep-water PTB Niushan (water
225 depth of >200 m) section is more distal to that of the shallow-water sections (0-50 m; Meishan

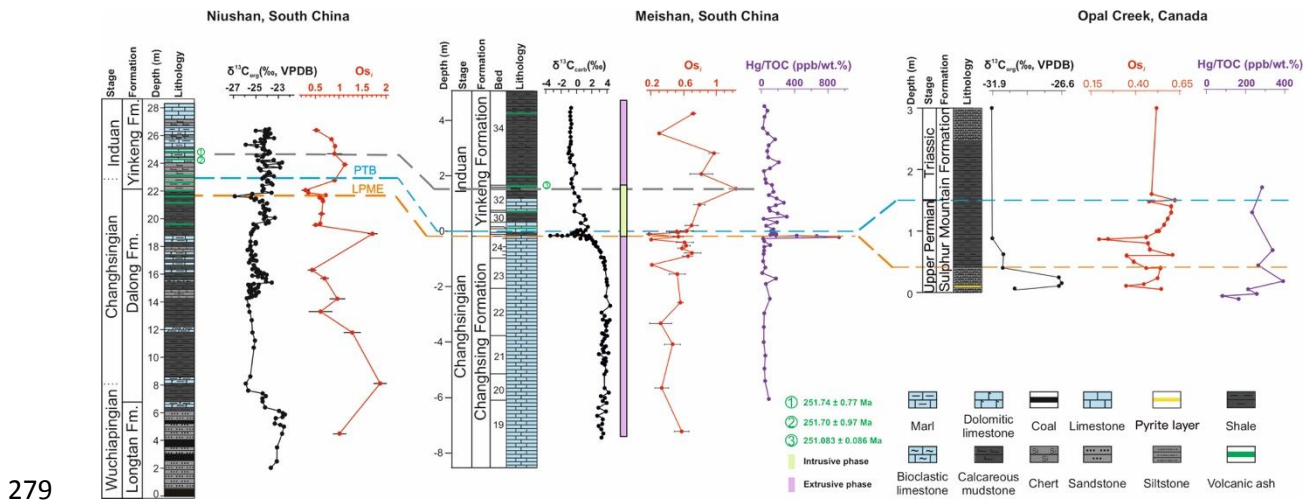
226 / Opal Creek) (Fig. 1) and therefore should reflect a more open marine signature (e.g., Rooney
227 et al., 2016; Jones et al., 2020). Thus, the Os isotope profile from the deep-water PTB Niushan
228 section, coupled with published data from shallow-water PTB sections, provides a more
229 comprehensive understanding of the global marine Os isotope record across the EPME event
230 (Schoepfer et al., 2013; Zhao et al., 2015; Georgiev et al., 2015; Liu et al., 2020b).

231 An unradiogenic shift in the Os_i composition from ~ 0.6 to 0.3 is found immediately
232 above the mass extinction interval (EPME, Fig. 2). In theory, the unradiogenic Os isotope shift
233 could be driven by increased input of unradiogenic Os from weathering of magmatic rocks
234 and/or a meteorite impact (Peucker-Ehrenbrink and Ravizza, 2000). However, there is a lack
235 of any convincing evidence for a meteorite impact (Shen et al., 2019b). Considering the
236 volcanic ash layers found in the Niushan section and the studies that have demonstrated the
237 intensive volcanic activity through the Late Permian and Early Triassic (e.g. Payne and Kump,
238 2007; Saunders and Reichow, 2009; Burgess et al., 2014; Burgess and Bowring, 2015; Burgess
239 et al., 2017; Liu et al., 2017; Wang et al., 2018; Shen et al., 2019a; Shen et al., 2019b),
240 magmatic activity is a more reasonable interpretation for the unradiogenic Os isotope excursion,
241 possibly linked with intensive volcanism in South China (e.g. Korte and Kozur, 2010; Yin and
242 Song, 2013; Liu et al., 2020b). The Os isotope data here provide further insights into the pattern
243 of the volcanism, and the temporal relationship between volcanism and the mass extinction
244 event. In the Niushan section, an unradiogenic osmium isotope shift is only detected after the
245 EPME, which is in contrast to the Meishan section that exhibits abrupt and intense
246 unradiogenic shifts in Os_i both pre- and post- the mass extinction event (Liu et al., 2020b). We
247 cannot rule out the possibility that the lack of unradiogenic Os_i shift before the mass extinction
248 interval at the Niushan section could have been missed in our sampling approach, however, the
249 interval around the PTB was sampled at a high resolution of ~ 10 cm, which is comparable to
250 that of the Meishan section. High precision Zircon U-Pb geochronology (CA-ID-TIMS)

251 suggests the Siberian Traps shift from extrusive eruption before the mass extinction to intrusive
252 magmatism during the mass extinction interval, and then back to extrusive eruption (Burgess
253 et al., 2017). The unradiogenic Os isotope excursions thus might correlate with the extrusive
254 phases of the Siberian Traps and the subsequent weathering of the mafic extrusive units.

255 Unfortunately, sample material for the exact sample that exhibits the largest negative
256 carbon isotope value (NS-107) of the Niushan section is no longer available. However, samples
257 immediately below sample NS-107 show no unradiogenic shift in Os_i , whereas the carbon
258 isotope values have already started to decline (Fig. 2). Nevertheless, the unradiogenic shift in
259 Os_i post the mass extinction interval is detected in both the Niushan and Meishan sections (Fig.
260 3). A previous study has attributed the difference in the Os isotope profiles between different
261 sections to different magnitude in the volcanic events that are responsible for the Os isotope
262 excursion(s) (Liu et al., 2019b). Those pulses of volcanism that preceded the mass extinction
263 event may be smaller in scale than that post the mass extinction event, and thus the later pulse
264 of volcanism is more widely recorded in the Os isotope oceanic record than that of the earlier
265 volcanic events. It is also possible that the volcanic activity occurred in a more terrestrial
266 location and thus not recorded in the deep-water column, and/or the unradiogenic Os isotope
267 shift identified post EPME in the Niushan section reflects the weathering of the basalt that
268 happened several tens of thousands of years after the volcanism. The latter is also supported
269 by Hg records from both the Meishan and Opal Creek sections that exhibit Hg/TOC anomalies
270 that are generally shown in the intervals below or within the EPME interval, which resulted
271 from synchronous Hg emission during volcanism (Fig. 3; Grasby et al., 2017; Wang et al.,
272 2018; Shen et al., 2019a). The fact that the Niushan section shows a smaller unradiogenic Os_i
273 shift than those recorded in sections representative of a slope depositional environment
274 (Meishan and Opal Creek) suggests that more open ocean deep-water settings were less
275 affected by volcanic activities, and corroborates the deep-water migration of foraminifers

276 around the PTB (Liu et al., 2020c). The latter is driven by toxic compounds released from the
 277 Siberian Traps and other volcanic activities in the shallow waters around the Tethys Ocean
 278 (Liu et al., 2020c).



279
 280 **Figure 3.** Correlation of Os_i from the Niushan section, the Meishan section and the Opal Creek
 281 (Canada) section. The Niushan $\delta^{13}C_{org}$ data are from Liao et al. (2016a). The Opal Creek
 282 section Os_i data are from Schoepfer et al. (2013) and Georgiev et al. (2015); $\delta^{13}C_{org}$ data from
 283 Gerogiev et al. (2015); Hg/TOC data from Shen et al. (2019a); and the uppermost $\delta^{13}C_{org}$ and
 284 Os_i data points represent the average value of all five Triassic samples. The Meishan section
 285 $\delta^{13}C_{carb}$ data from Shen et al. (2011), Os_i data from Liu et al. (2020b), Hg/TOC data from Wang
 286 et al. (2018) and Grasby et al. (2017). Age in the Meishan section is from CA-TIMS U-Pb
 287 zircon dated volcanic ash bed (Burgess et al., 2014). Ages in the Niushan section are LA-ICP-
 288 MS U-Pb zircon dated volcanic ash beds (Liao et al., 2016a; 2016b).

289 Above the unradiogenic shift, the Os_i values show an increase to more radiogenic
 290 values, peaking at 1.14, in the Niushan section (Fig. 2). In theory, the increase in Os_i can be
 291 caused by either reduced unradiogenic Os flux or increased radiogenic Os input from
 292 continental weathering to the water column. Given the active volcanism at this time, invoking
 293 an enhanced weathering scenario may be more appropriate to interpret the Os_i trend observed

294 at Niushan. A trend to more radiogenic Os_i following volcanism has also been reported for the
295 shallow-water Meishan section (Fig. 3). In the Meishan section, the Os_i shift to ~ 1.25 from
296 ~ 0.6 , which is slightly larger than the Os isotope value of 1.14 from the Niushan section (Liu
297 et al., 2020b). A previous study has suggested that in the near-shore regions, the marine
298 residence time of Os, that is, the amount of Os in seawater reservoir divided by the sum of
299 input or output fluxes, will be considerably shorter than the accepted value of *c.* 10^4 yr (e.g.
300 Paquay and Ravizza, 2012; Rooney et al., 2016). The more radiogenic Os_i at Meishan thus may
301 reflect its more proximal setting relative to Niushan, and as a result the increased radiogenic
302 Os flux might be slightly lower than previously estimated (Liu et al., 2020b). At steady state,
303 the seawater osmium isotope composition is determined by the mixing of radiogenic Os input
304 (1.4) and unradiogenic Os input (0.12) given by:

$$305 \quad R_{sw} = (M_u * R_u + M_r * R_r) \quad (1)$$

306 Where R_{sw} , R_u and R_r denote the Os isotope compositions of seawater, unradiogenic input and
307 radiogenic input; M_u and M_r represent the mass of unradiogenic Os input and radiogenic Os
308 input respectively. Assuming a constant weathering input of radiogenic Os, the volcanic Os
309 flux is estimated to have increased ~ 8 times, based on the Os isotope data from the Meishan
310 section (from 0.6 to 0.2; Liu et al., 2020b). However, using the data of this study (0.6 to 0.3),
311 the volcanic Os input increase is only ~ 2.7 times. Similarly, for the estimation of radiogenic
312 Os input from weathering, with the assumption of a stable unradiogenic Os input, Os isotope
313 data from the Meishan section suggest a ~ 9 times increase (Liu et al., 2020b). In contrast, Os
314 data from the Niushan section yield an increase of radiogenic Os flux by ~ 5 times (compared
315 with ~ 9 times by using a Os_i value of 1.2 from the Meishan section).

316 The Os_i values then fall from 1.14 to 0.5 above the PTB (Fig. 2). This unradiogenic
317 Os_i shift likely reflects decreasing weathering intensity, as excessive greenhouse volatiles were

318 mitigated by silicate weathering. This is earlier than that inferred from the Sr isotope data,
319 which indicates enhanced weathering until the late Early Triassic (Song et al., 2015). However,
320 Os has a considerably shorter oceanic residence time than Sr (10 kyr vs. 2 Ma). Thus, the Os
321 isotope data would be expected to show a decrease in the Os_i prior to Sr in response to the
322 decreased weathering above the PTB.

323 5.4 Implications for using $^{187}Os/^{188}Os$ for paleoclimate research

324 The $^{187}Os/^{188}Os$ composition of sedimentary units has been widely applied to infer the
325 Os-isotope composition of the water column at the time of deposition, and moreover to infer
326 the paleogeography / paleoceanography (e.g. Cohen, 2004; Turgeon and Creaser, 2008; Tejada
327 et al., 2009; Georgiev et al., 2011; Peucker-Ehrenbrink and Ravizza, 2012; Dickson et al.,
328 2015). Typically, the more proximal shallow-water sections generally have more radiogenic
329 Os isotope values compared to that of deep-water sections, due to elevated terrestrial Os input
330 with radiogenic Os isotope compositions and/or limited seawater exchange (e.g., Porter et al.,
331 2014; Rooney et al., 2016; Jones et al., 2020). Further, the Os isotope record from near-shore
332 and shelf/slope sections tend to exhibit larger signal excursions relative to those recovered from
333 deep-water sections (e.g., Jones et al., 2020). A similar scenario is also shown with the
334 Paleocene–Eocene thermal maximum initial Os isotope records. For example, the Millville
335 section, which is a near-shore expanded section, has a larger unradiogenic Os isotope
336 composition shift (~ 0.08) compared with most shelf sections that show unradiogenic Os
337 isotope composition shift of ~ 0.05 (Dickson et al., 2015; Liu et al., 2019a). Whereas, the
338 pelagic section at Blake Nose (ODP Hole 1051 B) only shows a nominal Os isotope
339 composition shift (~ 0.01), which is within analytical uncertainty of the Os isotope
340 measurement (Liu et al., 2019a). Another example is the Jurassic Toarcian Oceanic Anoxic
341 Event (T-OAE) that describes a radiogenic osmium isotope shift in response to enhanced
342 weathering. In the near-shore section of Yorkshire (UK), Os isotope increase by ~ 0.7 (Cohen

343 et al., 2004). Whereas for the more open marine sections of Mochras (UK), East Tributary
344 (North America), and Sakuraguchi-dani (Japan) excursions only increase by $\sim 0.3-0.4$ (Percival
345 et al., 2016; Them et al., 2017; Kemp et al., 2020).

346 In addition to tracking volcanism and/or extraterrestrial impact events, as well as
347 weathering signals, osmium isotopes have also been used to quantify the scale of the event,
348 and even the size of the impactor (if the type of the impactor is known) (Dickson et al., 2015;
349 Liu et al., 2019a; Paquay et al., 2008). Consequently, using Os isotope data from shallow-water
350 sections may yield an overestimation of the degree of the magmatism and/or weathering of
351 radiogenic Os, as well as the size of the impactor. As such, the Os isotope data from deep-water
352 sections might be a more reliable source of data for any numerical models. Thus, wherever
353 possible, such evaluations should be made with data from multiple sections to get a more
354 comprehensive understanding. A similar conclusion can also be drawn by using the T-OAE Os
355 isotope excursion data from near-shore section of Yorkshire (UK) (~ 0.7 Os_i change) and open
356 marine sections of Mochras (UK), Dotternhausen/Dormettingen (Germany), East Tributary
357 (North America), and Sakuraguchi-dani (Japan) ($\sim 0.3-0.4$ Os_i change) to estimate the
358 weathering intensity change over the T-OAE (Cohen et al., 2004; Them et al., 2017; van Acken
359 et al., 2019; Kemp et al., 2020).

360 Also noteworthy, massive volcanism associated with the EPME is also considered to
361 be associated with an increase in greenhouse gas emissions, which resulted in an increase in
362 silicate weathering and organic carbon burial (the negative feedback mechanism; Walker et al.,
363 1981; Jenkyns, 2010). As a result, the unradiogenic Os isotope shift signal driven by volcanism
364 might be dampened by the radiogenic Os input from increased weathering to some extent.

365 **6 Conclusions**

366 The Os isotope stratigraphy across the Permian–Triassic boundary interval of the
367 Niushan section suggests that volcanism and enhanced weathering are associated with the late
368 Permian mass extinction event. Unlike the Os isotope records from Meishan and Opal Creek,
369 the Os isotope data from the Niushan section show no unradiogenic Os isotope excursion
370 immediately before the mass extinction interval. The Niushan section does however exhibit an
371 unradiogenic Os isotope shift following the mass extinction interval. There is also a radiogenic
372 Os isotope shift signal detected above the unradiogenic Os isotope shift, which is interpreted
373 to be caused by enhanced weathering. Both the volcanism and weathering signals are smaller
374 relative to those reported from the Meishan and Opal Creek sections. As such, different
375 paleogeographic settings may record different magnitudes in the Os isotope excursions, and
376 thus any numerical evaluation using Os isotope stratigraphy to model geological events should
377 be treated carefully unless based on multiple sites and/or more open ocean records where
378 possible.

379 **Acknowledgements**

380 We would like to thank Prof. Jian Cao (Nanjing University) for providing the samples
381 for this study. For laboratory support we gratefully acknowledge Antonia Hofmann, Chris
382 Ottley, Geoff Nowell and Emma Ownsworth. We also acknowledge the TOTAL Endowment
383 Fund and the CUG Wuhan Dida Scholarship to DS, China Postdoctoral Science Foundation
384 (20M682934) and the University of Durham and China Scholarship Council to ZL. Finally, we
385 would like to thank David van Acken and one anonymous reviewer for their constructive
386 reviews that greatly improved the manuscript. Data available from an open-source online data
387 repository hosted at Mendeley Data (<http://dx.doi.org/10.17632/c3864dc938.1>).

388

389 **References**

- 390 Birck, J. L., M. R. Barman, and F. Capmas (1997), Re-Os Isotopic Measurements at the
391 Femtomole Level in Natural Samples, *Geostandards Newsletter*, 21(1), 19-27, doi:
392 <https://doi.org/10.1111/j.1751-908X.1997.tb00528.x>.
- 393 Burgess, S. D., S. Bowring, and S.-z. Shen (2014), High-precision timeline for Earth's most
394 severe extinction, *Proceedings of the National Academy of Sciences*, 111(9), 3316-3321,
395 doi: <https://doi.org/10.1073/pnas.1317692111>.
- 396 Burgess, S. D., and S. A. Bowring (2015), High-precision geochronology confirms voluminous
397 magmatism before, during, and after Earth's most severe extinction, *Science Advances*,
398 1(7), doi: <https://doi.org/10.1126/sciadv.1500470>.
- 399 Burgess, S. D., J. D. Muirhead, and S. A. Bowring (2017), Initial pulse of Siberian Traps sills
400 as the trigger of the end-Permian mass extinction, *Nature Communications*, 8(1), 164,
401 doi: <https://doi.org/10.1038/s41467-017-00083-9>.
- 402 Cao, C., G. D. Love, L. E. Hays, W. Wang, S. Shen, and R. E. Summons (2009),
403 Biogeochemical evidence for euxinic oceans and ecological disturbance presaging the
404 end-Permian mass extinction event, *Earth and Planetary Science Letters*, 281(3), 188-
405 201, doi: <http://dx.doi.org/10.1016/j.epsl.2009.02.012>.
- 406 Chen, J., et al. (2016), High-resolution SIMS oxygen isotope analysis on conodont apatite from
407 South China and implications for the end-Permian mass extinction, *Palaeogeography*,
408 *Palaeoclimatology*, *Palaeoecology*, 448, 26-38, doi:
409 <http://dx.doi.org/10.1016/j.palaeo.2015.11.025>.

410 Chu, D., et al. (2020), Ecological disturbance in tropical peatlands prior to marine Permian-
411 Triassic mass extinction, *Geology*, 48(3), 288-292, doi:
412 <https://doi.org/10.1130/g46631.1>.

413 Clarkson, M. O., S. A. Kasemann, R. A. Wood, T. M. Lenton, S. J. Daines, S. Richoz, F.
414 Ohnemüller, A. Meixner, S. W. Poulton, and E. T. Tipper (2015), Ocean acidification
415 and the Permo-Triassic mass extinction, *Science*, 348(6231), 229-232, doi:
416 <https://doi.org/10.1126/science.aaa0193>.

417 Cohen, A. S. (2004), The rhenium–osmium isotope system: applications to geochronological
418 and palaeoenvironmental problems, *Journal of the Geological Society*, 161(4), 729-734.
419 doi: <https://doi.org/10.1144/0016-764903-084>.

420 Cohen, A. S., A. L. Coe, S. M. Harding, and L. Schwark (2004), Osmium isotope evidence for
421 the regulation of atmospheric CO₂ by continental weathering, *Geology*, 32(2), 157-160.
422 doi: <https://doi.org/10.1130/G20158.1>.

423 Cohen, A. S., and F. G. Waters (1996), Separation of osmium from geological materials by
424 solvent extraction for analysis by thermal ionisation mass spectrometry, *Analytica*
425 *Chimica Acta*, 332(2–3), 269-275, doi:[http://dx.doi.org/10.1016/0003-2670\(96\)00226-](http://dx.doi.org/10.1016/0003-2670(96)00226-7)
426 [7](http://dx.doi.org/10.1016/0003-2670(96)00226-7).

427 Dal Corso, J., B. J. W. Mills, D. Chu, R. J. Newton, T. A. Mather, W. Shu, Y. Wu, J. Tong,
428 and P. B. Wignall (2020), Permo–Triassic boundary carbon and mercury cycling linked
429 to terrestrial ecosystem collapse, *Nature Communications*, 11(1), 2962, doi:
430 <http://dx.doi.org/10.1038/s41467-020-16725-4>.

431 Dickson, A. J., A. S. Cohen, A. L. Coe, M. Davies, E. A. Shcherbinina, and Y. O. Gavrillov
432 (2015), Evidence for weathering and volcanism during the PETM from Arctic Ocean

433 and Peri-Tethys osmium isotope records, *Palaeogeography, Palaeoclimatology,*
434 *Palaeoecology*, 438, 300-307, doi:<http://dx.doi.org/10.1016/j.palaeo.2015.08.019>.

435 Du Vivier, A. D. C., D. Selby, D. J. Condon, R. Takashima, and H. Nishi (2015), Pacific
436 $^{187}\text{Os}/^{188}\text{Os}$ isotope chemistry and U–Pb geochronology: Synchronicity of global Os
437 isotope change across OAE 2, *Earth and Planetary Science Letters*, 428, 204-216,
438 doi:<http://dx.doi.org/10.1016/j.epsl.2015.07.020>.

439 Du Vivier, A. D. C., D. Selby, B. B. Sageman, I. Jarvis, D. R. Gröcke, and S. Voigt (2014),
440 Marine $^{187}\text{Os}/^{188}\text{Os}$ isotope stratigraphy reveals the interaction of volcanism and ocean
441 circulation during Oceanic Anoxic Event 2, *Earth and Planetary Science Letters*, 389,
442 23-33, doi:<http://dx.doi.org/10.1016/j.epsl.2013.12.024>.

443 Erwin, D. H. (2006), *Extinction: how life on earth nearly ended 250 million years ago*,
444 Princeton University Press.

445 Garbelli, C., L. Angiolini, and S.-z. Shen (2017), Biomineralization and global change: A new
446 perspective for understanding the end-Permian extinction, *Geology*, 45(1), 19-22, doi:
447 <https://doi.org/10.1130/g38430.1>.

448 Georgiev, S., H. J. Stein, J. L. Hannah, B. Bingen, H. M. Weiss, and S. Piasecki (2011), Hot
449 acidic Late Permian seas stifle life in record time, *Earth and Planetary Science Letters*,
450 310(3), 389-400, doi:<https://doi.org/10.1016/j.epsl.2011.08.010>.

451 Georgiev, S. V., H. J. Stein, J. L. Hannah, C. M. Henderson, and T. J. Algeo (2015), Enhanced
452 recycling of organic matter and Os-isotopic evidence for multiple magmatic or
453 meteoritic inputs to the Late Permian Panthalassic Ocean, Opal Creek, Canada,
454 *Geochimica et Cosmochimica Acta*, 150, 192-210,
455 doi:<https://doi.org/10.1016/j.gca.2014.11.019>.

456 Georgiev, S. V., H. J. Stein, G. Yang, J. L. Hannah, M. E. Böttcher, K. Grice, A. I. Holman, S.
457 Turgeon, S. Simonsen, and C. Cloquet (2020), Late Permian–Early Triassic
458 environmental changes recorded by multi-isotope (Re-Os-N-Hg) data and trace metal
459 distribution from the Hovea-3 section, Western Australia, *Gondwana Research*, 88,
460 353-372, doi:<https://doi.org/10.1016/j.gr.2020.07.007>.

461 Grasby, S. E., W. Shen, R. Yin, J. D. Gleason, J. D. Blum, R. F. Lepak, J. P. Hurley, and B.
462 Beauchamp (2017), Isotopic signatures of mercury contamination in latest Permian
463 oceans, *Geology*, 45(1), 55-58, doi: <https://doi.org/10.1130/g38487.1>.

464 Grice, K., C. Cao, G. D. Love, M. E. Böttcher, R. J. Twitchett, E. Grosjean, R. E. Summons,
465 S. C. Turgeon, W. Dunning, and Y. Jin (2005), Photic zone euxinia during the Permian-
466 Triassic superanoxic event, *Science*, 307(5710), 706-709, doi:
467 <https://doi.org/10.1126/science.1104323>.

468 Harris, N. B., C. A. Mnich, D. Selby, and D. Korn (2013), Minor and trace element and Re–
469 Os chemistry of the Upper Devonian Woodford Shale, Permian Basin, west Texas:
470 Insights into metal abundance and basin processes, *Chemical Geology*, 356, 76-93,
471 doi:<http://dx.doi.org/10.1016/j.chemgeo.2013.07.018>.

472 Henderson, C.M., 1989. Absaroka Sequence—The Lower Absaroka Sequence: Upper
473 Carboniferous and Permian (Chapter 10). In: Ricketts, B. (Ed.), Basin Analysis— The
474 Western Canada Sedimentary Basin: Canadian Society of Petroleum Geologists Special
475 Publication, p. 203–217.

476 Hinojosa, J. L., S. T. Brown, J. Chen, D. J. DePaolo, A. Paytan, S.-z. Shen, and J. L. Payne
477 (2012), Evidence for end-Permian ocean acidification from calcium isotopes in
478 biogenic apatite, *Geology*, 40(8), 743-746, doi: <https://doi.org/10.1130/g33048.1>.

479 Hu, G., Z. Liao, L. Wang, J. Cao, and X. Tan (2019), Transient fluctuation in paleoclimate at
480 the end of Permian: New constraints from paleosol carbonates in the Erlongkou section,
481 Chongqing, southwestern China, *Journal of Asian Earth Sciences*, 173, 225-236,
482 doi:<https://doi.org/10.1016/j.jseaes.2019.01.027>.

483 Jenkyns, H. C. (2010), Geochemistry of oceanic anoxic events, *Geochemistry Geophysics*
484 *Geosystems*, 11(3), doi: <https://doi.org/ArtnQ0300410.1029/2009gc002788>.

485 Jin, Y., Y. Wang, C. Henderson, B. R. Wardlaw, S. Shen, and C. Cao (2006), The Global
486 Boundary Stratotype Section and Point (GSSP) for the base of Changhsingian Stage
487 (Upper Permian), *Episodes*, 29(3), 175-182.

488 Joachimski, M. M., X. Lai, S. Shen, H. Jiang, G. Luo, B. Chen, J. Chen, and Y. Sun (2012),
489 Climate warming in the latest Permian and the Permian–Triassic mass extinction,
490 *Geology*, 40(3), 195-198, doi: <https://doi.org/10.1130/g32707.1>.

491 Jones, M. M., B. B. Sageman, D. Selby, B. R. Jicha, B. S. Singer, and A. L. Titus (2020),
492 Regional chronostratigraphic synthesis of the Cenomanian-Turonian Oceanic Anoxic
493 Event 2 (OAE2) interval, Western Interior Basin (USA): New Re-Os
494 chemostratigraphy and $^{40}\text{Ar}/^{39}\text{Ar}$ geochronology, *GSA Bulletin*, doi:
495 <https://doi.org/10.1130/b35594.1>.

496 Kemp, D. B., D. Selby, and K. Izumi (2020), Direct coupling between carbon release and
497 weathering during the Toarcian oceanic anoxic event, *Geology*, doi:
498 <https://doi.org/10.1130/g47509.1>.

499 Kendall, B. S., R. A. Creaser, G. M. Ross, and D. Selby (2004), Constraints on the timing of
500 Marinoan “Snowball Earth” glaciation by ^{187}Re – ^{187}Os dating of a Neoproterozoic, post-

501 glacial black shale in Western Canada, *Earth and Planetary Science Letters*, 222(3),
502 729-740, doi:<https://doi.org/10.1016/j.epsl.2004.04.004>.

503 Korte, C., and H. W. Kozur (2010), Carbon-isotope stratigraphy across the Permian–Triassic
504 boundary: A review, *Journal of Asian Earth Sciences*, 39(4), 215-235,
505 doi:<https://doi.org/10.1016/j.jseaes.2010.01.005>.

506 Liao, Z., W. Hu, J. Cao, X. Wang, S. Yao, and Y. Wan (2016a), Permian–Triassic boundary
507 (PTB) in the Lower Yangtze Region, southeastern China: A new discovery of deep-
508 water archive based on organic carbon isotopic and U–Pb geochronological studies,
509 *Palaeogeography, Palaeoclimatology, Palaeoecology*, 451, 124-139,
510 doi:<http://dx.doi.org/10.1016/j.palaeo.2016.03.004>.

511 Liao, Z., W. Hu, J. Cao, X. Wang, S. Yao, H. Wu, and Y. Wan (2016b), Heterogeneous
512 volcanism across the Permian–Triassic Boundary in South China and implications for
513 the Latest Permian Mass Extinction: New evidence from volcanic ash layers in the
514 Lower Yangtze Region, *Journal of Asian Earth Sciences*, 127, 197-210,
515 doi:<http://dx.doi.org/10.1016/j.jseaes.2016.06.003>.

516 Liu, S.-A., H. Wu, S.-z. Shen, G. Jiang, S. Zhang, Y. Lv, H. Zhang, and S. Li (2017), Zinc
517 isotope evidence for intensive magmatism immediately before the end-Permian mass
518 extinction, *Geology*, 45(4), 343-346, doi: <https://doi.org/10.1130/g38644.1>.

519 Liu, Z., D. E. Horton, C. Tabor, B. B. Sageman, L. M. E. Percival, B. C. Gill, and D. Selby
520 (2019a), Assessing the Contributions of comet impact and volcanism toward the
521 climate perturbations of the Paleocene-Eocene Thermal Maximum, *Geophysical
522 Research Letters*, 46(24), 14798-14806, doi: <https://doi.org/10.1029/2019gl084818>.

523 Liu, Z., D. Selby, P. C. Hackley, and D. J. Over (2020a), Evidence of wildfires and elevated
524 atmospheric oxygen at the Frasnian–Famennian boundary in New York (USA):

525 Implications for the Late Devonian mass extinction, *GSA Bulletin*, doi:
526 <https://doi.org/10.1130/b35457.1>.

527 Liu, Z., D. Selby, H. Zhang, and S. Shen (2020b), Evidence for volcanism and weathering
528 during the Permian-Triassic mass extinction from Meishan (South China) osmium
529 isotope record, *Palaeogeography, Palaeoclimatology, Palaeoecology*, 553, 109790,
530 doi:<https://doi.org/10.1016/j.palaeo.2020.109790>.

531 Liu, X., H. Song, D. P. G. Bond, J. Tong, and M. J. Benton (2020c), Migration controls
532 extinction and survival patterns of foraminifers during the Permian-Triassic crisis in
533 South China, *Earth-Science Reviews*, 209, 103329, doi:
534 <https://doi.org/10.1016/j.earscirev.2020.103329>.

535 Liu, Z., D. Selby, H. Zhang, Q. Zheng, S. Shen, B. B. Sageman, S. E. Grasby, and B.
536 Beauchamp (2019b), Osmium-isotope evidence for volcanism across the
537 Wuchiapingian–Changhsingian boundary interval, *Chemical Geology*, 529, 119313,
538 doi:<https://doi.org/10.1016/j.chemgeo.2019.119313>.

539 Paquay, F. S., and G. Ravizza (2012), Heterogeneous seawater $^{187}\text{Os}/^{188}\text{Os}$ during the Late
540 Pleistocene glaciations, *Earth and Planetary Science Letters*, 349–350, 126-138,
541 doi:<http://dx.doi.org/10.1016/j.epsl.2012.06.051>.

542 Paquay, F. S., G. E. Ravizza, T. K. Dalai, and B. Peucker-Ehrenbrink (2008), Determining
543 chondritic impactor size from the marine osmium isotope record, *Science*, 320(5873),
544 214-218, doi: <https://doi.org/10.1126/science.1152860>.

545 Pašava, J., S. Oszczepalski, and A. Du (2010), Re–Os age of non-mineralized black shale from
546 the Kupferschiefer, Poland, and implications for metal enrichment, *Mineralium*
547 *Deposita*, 45(2), 189-199, doi: <https://doi.org/10.1007/s00126-009-0269-8>.

548 Payne, J. L., and L. R. Kump (2007), Evidence for recurrent Early Triassic massive volcanism
549 from quantitative interpretation of carbon isotope fluctuations, *Earth and Planetary*
550 *Science Letters*, 256(1), 264-277, doi:<https://doi.org/10.1016/j.epsl.2007.01.034>.

551 Percival, L. M. E., A. S. Cohen, M. K. Davies, A. J. Dickson, S. P. Hesselbo, H. C. Jenkyns,
552 M. J. Leng, T. A. Mather, M. S. Storm, and W. Xu (2016), Osmium isotope evidence
553 for two pulses of increased continental weathering linked to Early Jurassic volcanism
554 and climate change, *Geology*, 44(9), 759-762, doi: <https://doi.org/10.1130/G37997.1>.

555 Peucker-Ehrenbrink, B., and B.-m. Jahn (2001), Rhenium-osmium isotope systematics and
556 platinum group element concentrations: Loess and the upper continental crust,
557 *Geochemistry, Geophysics, Geosystems*, 2(10), n/a-n/a, doi:
558 <https://doi.org/10.1029/2001GC000172>.

559 Peucker-Ehrenbrink, B., and G. Ravizza (2000), The marine osmium isotope record, *Terra*
560 *Nova*, 12(5), 205-219, doi: <https://doi.org/10.1046/j.1365-3121.2000.00295.x>.

561 Peucker-Ehrenbrink, B., and G. Ravizza (2012), Osmium Isotope Stratigraphy, in *The*
562 *Geologic Time Scale*, edited by F. M. Gradstein, J. G. Ogg, M. D. Schmitz and G. M.
563 Ogg, pp. 145-166, Elsevier, Boston, doi: [https://doi.org/10.1016/b978-0-444-59425-](https://doi.org/10.1016/b978-0-444-59425-9.00008-1)
564 [9.00008-1](https://doi.org/10.1016/b978-0-444-59425-9.00008-1).

565 Porter, S. J., P. L. Smith, A. H. Caruthers, P. Hou, D. R. Gröcke, and D. Selby (2014), New
566 high resolution geochemistry of Lower Jurassic marine sections in western North
567 America: A global positive carbon isotope excursion in the Sinemurian?, *Earth and*
568 *Planetary Science Letters*, 397, 19-31, doi:<https://doi.org/10.1016/j.epsl.2014.04.023>.

569 Rooney, A. D., D. M. Chew, and D. Selby (2011), Re–Os geochronology of the
570 Neoproterozoic–Cambrian Dalradian Supergroup of Scotland and Ireland: Implications

571 for Neoproterozoic stratigraphy, glaciations and Re–Os systematics, *Precambrian*
572 *Research*, 185(3–4), 202-214, doi:<http://dx.doi.org/10.1016/j.precamres.2011.01.009>.

573 Rooney, A. D., D. Selby, J. M. Lloyd, D. H. Roberts, A. Lückge, B. B. Sageman, and N. G.
574 Prouty (2016), Tracking millennial-scale Holocene glacial advance and retreat using
575 osmium isotopes: Insights from the Greenland ice sheet, *Quaternary Science Reviews*,
576 *138*, 49-61, doi:<http://dx.doi.org/10.1016/j.quascirev.2016.02.021>.

577 Rotich, E. K., M. R. Handler, S. Naeher, D. Selby, C. J. Hollis, and R. Sykes (2020), Re–Os
578 geochronology and isotope systematics, and organic and sulfur geochemistry of the
579 middle–late Paleocene Waipawa Formation, New Zealand: Insights into early
580 Paleogene seawater Os isotope composition, *Chemical Geology*, *536*, 119473,
581 doi:<https://doi.org/10.1016/j.chemgeo.2020.119473>.

582 Saunders, A., and M. Reichow (2009), The Siberian Traps and the End-Permian mass
583 extinction: a critical review, *Chinese Science Bulletin*, *54*(1), 20-37, doi:
584 <https://doi.org/10.1007/s11434-008-0543-7>.

585 Schoepfer, S. D., C. M. Henderson, G. H. Garrison, J. Foriel, P. D. Ward, D. Selby, J. C. Hower,
586 T. J. Algeo, and Y. Shen (2013), Termination of a continent-margin upwelling system
587 at the Permian–Triassic boundary (Opal Creek, Alberta, Canada), *Global and Planetary*
588 *Change*, *105*, 21-35, doi:<http://dx.doi.org/10.1016/j.gloplacha.2012.07.005>.

589 Selby, D., and R. A. Creaser (2003), Re–Os geochronology of organic rich sediments: an
590 evaluation of organic matter analysis methods, *Chemical Geology*, *200*(3–4), 225-240,
591 doi:[http://dx.doi.org/10.1016/S0009-2541\(03\)00199-2](http://dx.doi.org/10.1016/S0009-2541(03)00199-2).

592 Selby, D., R. A. Creaser, and M. G. Fowler (2007), Re–Os elemental and isotopic systematics
593 in crude oils, *Geochimica et Cosmochimica Acta*, *71*(2), 378-386,
594 doi:<https://doi.org/10.1016/j.gca.2006.09.005>.

595 Shen, J., T. J. Algeo, Q. Hu, G. Xu, L. Zhou, and Q. Feng (2013), Volcanism in South China
596 during the Late Permian and its relationship to marine ecosystem and environmental
597 changes, *Global and Planetary Change*, 105, 121-134,
598 doi:<https://doi.org/10.1016/j.gloplacha.2012.02.011>.

599 Shen, J., J. Chen, T. J. Algeo, S. Yuan, Q. Feng, J. Yu, L. Zhou, B. O'Connell, and N. J.
600 Planavsky (2019a), Evidence for a prolonged Permian–Triassic extinction interval from
601 global marine mercury records, *Nature Communications*, 10(1), 1563, doi:
602 <https://doi.org/10.1038/s41467-019-09620-0>.

603 Shen, S., et al. (2019b), *A sudden end-Permian mass extinction in South China*, GSA Bulletin,
604 doi: <https://doi.org/10.1130/B31909.1>.

605 Shen, S., et al. (2019c), Permian integrative stratigraphy and timescale of China, *Science*
606 *China-Earth Sciences*, 62(1), 154-188, doi: [https://doi.org/10.1007/s11430-017-9228-](https://doi.org/10.1007/s11430-017-9228-4)
607 4.

608 Shen, S.-z., et al. (2011), Calibrating the End-Permian Mass Extinction, *Science*, 334(6061),
609 1367-1372, doi: <https://doi.org/10.1126/science.1213454>.

610 Smoliar, M. I., R. J. Walker, and J. W. Morgan (1996), Re-Os ages of group IIA, IIIA, IVA,
611 and IVB iron meteorites, *Science*, 271(5252), 1099.
612 <https://doi.org/10.1126/science.271.5252.1099>.

613 Song, H., et al. (2015), Integrated Sr isotope variations and global environmental changes
614 through the Late Permian to early Late Triassic, *Earth and Planetary Science Letters*,
615 424, 140-147, doi:<https://doi.org/10.1016/j.epsl.2015.05.035>.

616 Song, H., et al. (2021), Conodont calcium isotopic evidence for multiple shelf acidification
617 events during the Early Triassic, *Chemical Geology*, 562, 120038, doi:
618 <https://doi.org/10.1016/j.chemgeo.2020.120038>.

619 Sperling, E. A., A. D. Rooney, L. Hays, V. N. Sergeev, N. G. Vorob'eva, N. D. Sergeeva, D.
620 Selby, D. T. Johnston, and A. H. Knoll (2014), Redox heterogeneity of subsurface
621 waters in the Mesoproterozoic ocean, *Geobiology*, 12(5), 373-386, doi:
622 <https://doi.org/10.1111/gbi.12091>.

623 Sun, H., Y. Xiao, Y. Gao, G. Zhang, J. F. Casey, and Y. Shen (2018), Rapid enhancement of
624 chemical weathering recorded by extremely light seawater lithium isotopes at the
625 Permian–Triassic boundary, *Proceedings of the National Academy of Sciences*, 115(15),
626 3782-3787, doi: <https://doi.org/10.1073/pnas.1711862115>.

627 Sun, Y., M. M. Joachimski, P. B. Wignall, C. Yan, Y. Chen, H. Jiang, L. Wang, and X. Lai
628 (2012), Lethally hot temperatures during the early Triassic greenhouse, *Science*,
629 338(6105), 366-370, doi: <https://doi.org/10.1126/science.1224126>.

630 Tejada, M. L. G., J. Kuroda, K. Suzuki, N. Ohkouchi, T. Sakamoto, Y. Tatsumi, R. Coccioni,
631 and J. J. Mahoney (2009), Ontong Java Plateau eruption as a trigger for the early Aptian
632 oceanic anoxic event, *Geology*, 37(9), 855-858, doi:
633 <https://doi.org/10.1130/G25763A.1>.

634 Them, T. R., B. C. Gill, D. Selby, D. R. Gröcke, R. M. Friedman, and J. D. Owens (2017),
635 Evidence for rapid weathering response to climatic warming during the Toarcian
636 Oceanic Anoxic Event, *Scientific Reports*, 7(1), 5003, doi:
637 <https://doi.org/10.1038/s41598-017-05307-y>.

638 Turgeon, S. C., and R. A. Creaser (2008), Cretaceous oceanic anoxic event 2 triggered by a
639 massive magmatic episode, *Nature*, 454(7202), 323-326, doi:
640 <https://doi.org/10.1038/nature07076>.

641 van Acken, D., T. Tütken, J. S. Daly, A. Schmid-Röhl, and P. J. Orr (2019), Rhenium - osmium
642 geochronology of the Toarcian Posidonia Shale, SW Germany, *Palaeogeography*,
643 *Palaeoclimatology*, *Palaeoecology*, 534, 109294,
644 doi:<https://doi.org/10.1016/j.palaeo.2019.109294>.

645 Walker, J. C. G., P. B. Hays, and J. F. Kasting (1981), A negative feedback mechanism for the
646 long-term stabilization of Earth's surface temperature, *Journal of Geophysical*
647 *Research: Oceans*, 86(C10), 9776-9782, doi:
648 <https://doi.org/10.1029/JC086iC10p09776>.

649 Wang, X., P. A. Cawood, H. Zhao, L. Zhao, S. E. Grasby, Z.-Q. Chen, P. B. Wignall, Z. Lv,
650 and C. Han (2018), Mercury anomalies across the end Permian mass extinction in South
651 China from shallow and deep water depositional environments, *Earth and Planetary*
652 *Science Letters*, 496, 159-167, doi:<https://doi.org/10.1016/j.epsl.2018.05.044>.

653 Wang, Y., and Y. Jin (2000), Permian palaeogeographic evolution of the Jiangnan Basin, South
654 China, *Palaeogeography*, *Palaeoclimatology*, *Palaeoecology*, 160(1), 35-44,
655 doi:[https://doi.org/10.1016/S0031-0182\(00\)00043-2](https://doi.org/10.1016/S0031-0182(00)00043-2).

656 Wignall, P. B., and R. J. Twitchett (1996), Oceanic Anoxia and the End Permian Mass
657 Extinction, *Science*, 272(5265), 1155-1158, doi:
658 <https://doi.org/10.1126/science.272.5265.1155>.

659 Xu, G., J. L. Hannah, B. Bingen, S. Georgiev, and H. J. Stein (2012), Digestion methods for
660 trace element measurements in shales: Paleoredox proxies examined, *Chemical*
661 *Geology*, 324-325, 132-147, doi:<https://doi.org/10.1016/j.chemgeo.2012.01.029>.

662 Yamashita, Y., Y. Takahashi, H. Haba, S. Enomoto, and H. Shimizu (2007), Comparison of
663 reductive accumulation of Re and Os in seawater–sediment systems, *Geochimica et*
664 *Cosmochimica Acta*, 71(14), 3458-3475, doi:<https://doi.org/10.1016/j.gca.2007.05.003>.

665 Yang, G., J. Chen, A. Du, W. Qu, and G. Yu (2004), *Re-Os dating of Mo-bearing black shale*
666 *of the Laoyaling deposit, Tongling, Anhui Province, China*, 49, 1396-1400, doi:
667 <https://doi.org/10.1360/03wd0325>.

668 Yin H.F., Zhang, K.X., Tong, J.N., Yang, Z.Y. and W, S.B. (2001), The Global Stratotype
669 Section and Point (GSSP) of the Permian-Triassic Boundary, *Episodes*, 24, 102-114.

670 Yin, H., and H. Song (2013), Mass extinction and Pangea integration during the Paleozoic-
671 Mesozoic transition, *Science China Earth Sciences*, 56(11), 1791-1803, doi:
672 <https://doi.org/10.1007/s11430-013-4624-3>.

673 Zhao, H., Li, C., Jiang, X.J., Zhou, L.M., Li, X.W., Qu, W.J. and Du, A.D., 2015. Enrichment
674 Mechanism of Re-Os in Limestone from Changxing Permian-Triassic Boundary in
675 Zhejiang. *Acta Geologica Sinica*, 89, 1783-1791. (in Chinese)

676 Ziegler, A.M., Hulver, M.L., Rowley, D.B., 1997, Permian world topography and climate. In:
677 Martini, I.P. (Ed.), *Late Glacial and Postglacial Environmental Changes–Quaternary,*
678 *Carboniferous–Permian and Proterozoic*. Oxford University Press, New York, p. 111–
679 146.

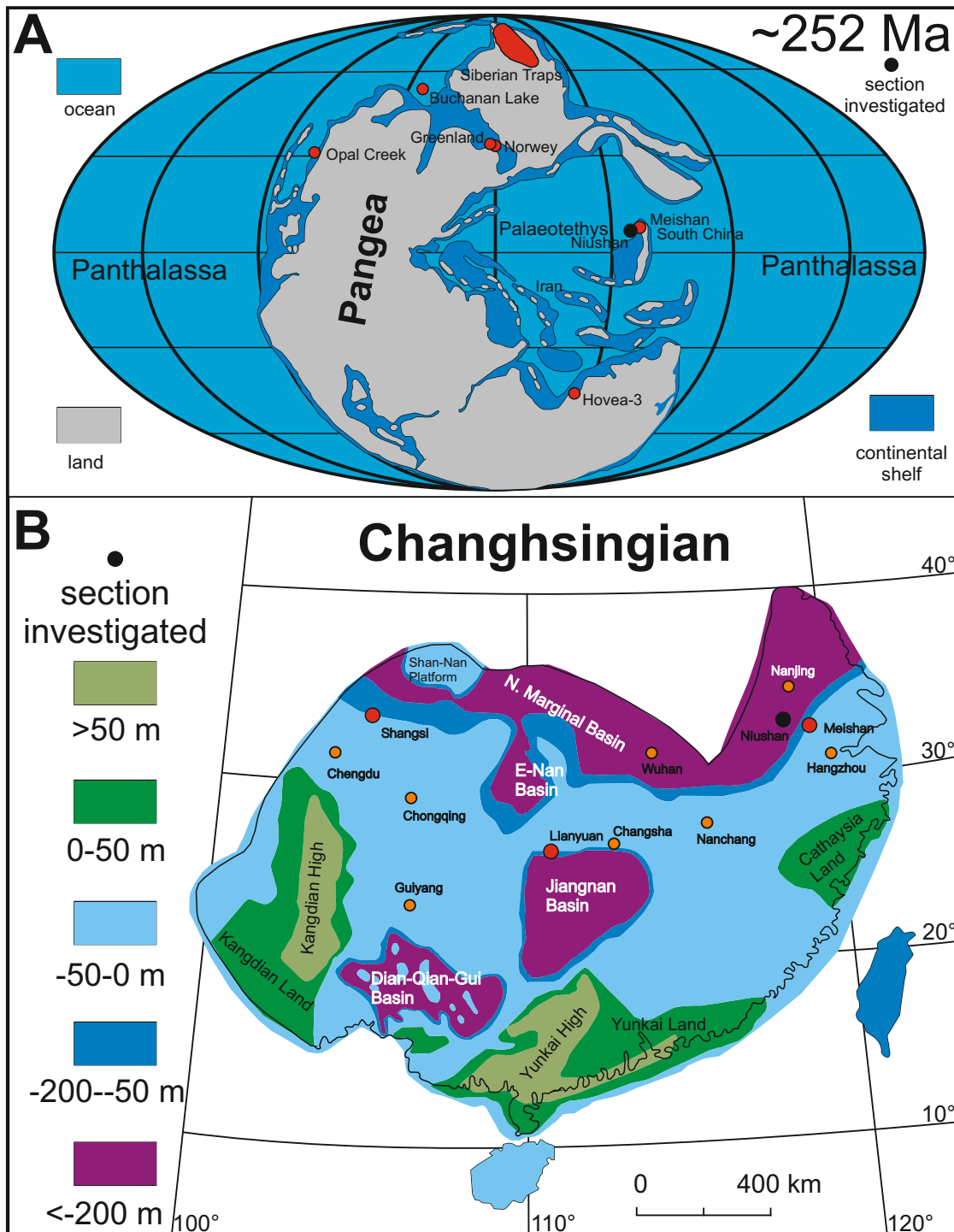
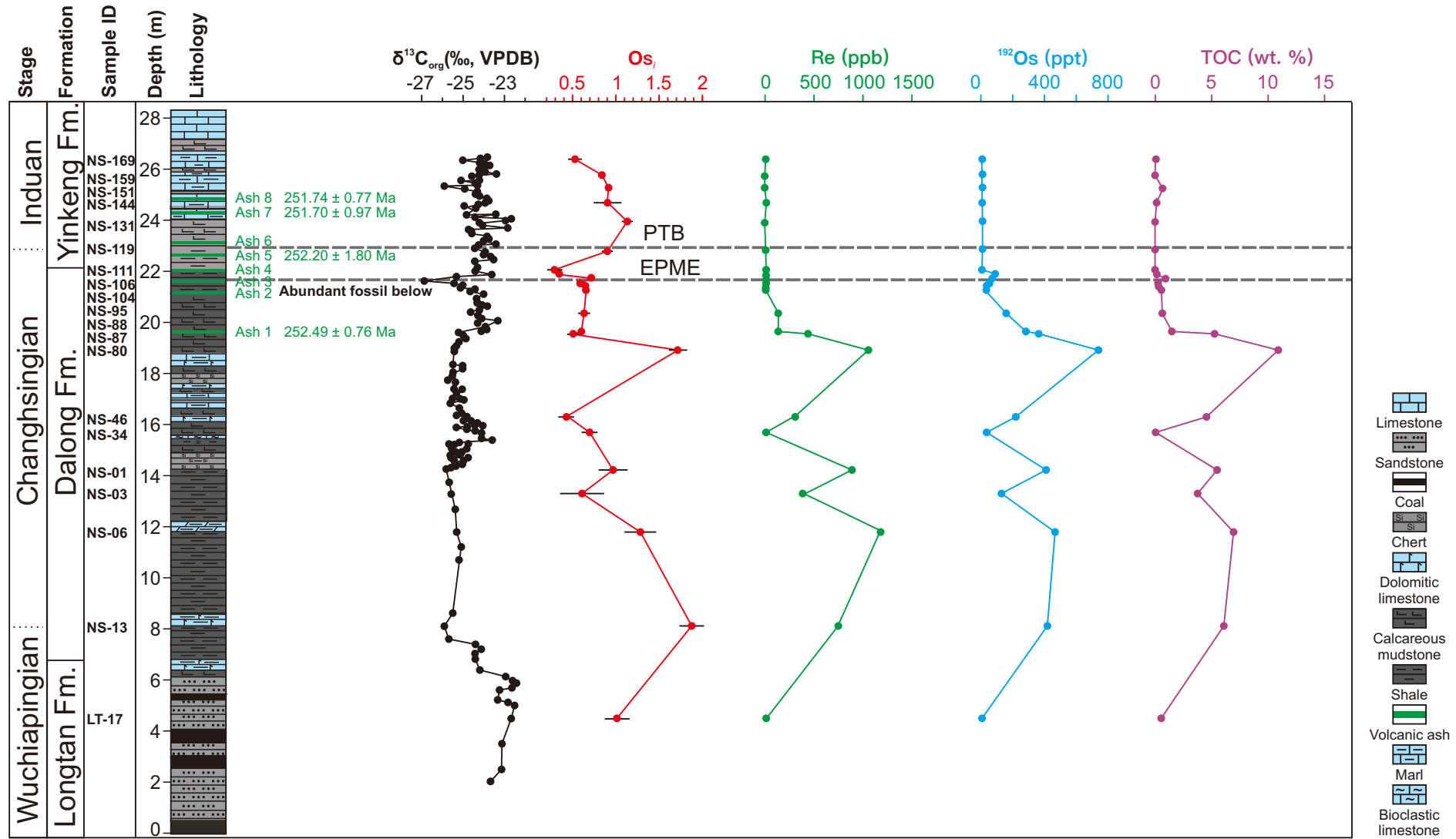
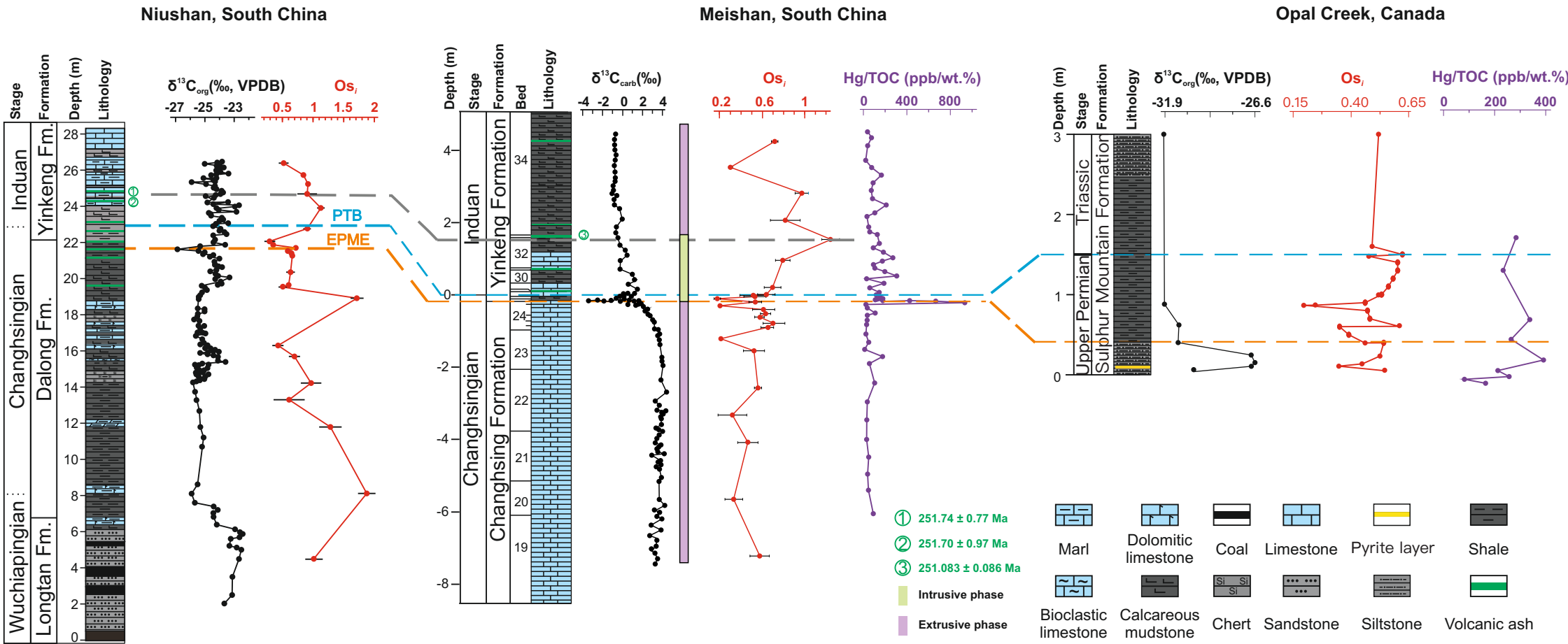


Figure 2





Conflict of Interest

The authors declare no conflict of interest. This manuscript has not been submitted and will not be submitted to any other journals while it is under review for *Global and Planetary Change*.



Click here to access/download
e-Component
2021 Liu et al .xlsx

